Available Power and Collective Scattering in Galactic Rotation Curves

Todd J. Desiato

Manuscript version 0.6 · 25 October 2026

Independent researcher, Statesville, North Carolina, USA
Correspondence: mainengineering@gmail.com · ORCID: 0000-0002-7514-0169

Abstract

What change in the electromagnetic exchange supporting matter would produce the orbital speeds measured in a galaxy? Operational Quantum Gravity (OQG) connects this question to gravity through its supporting-power theorem: the balanced exchange fixes complete material energy, and a spatial change in that energy produces gravitational motion. We apply this correspondence, within its stated material conditions, to three published galactic rotation curves. Their reconstructed inner-to-outer power deficits are 0.0632, 0.990, and 4.28 parts per million for DDO 154, NGC 2403, and NGC 7814. Relative to the adopted gas and stellar contributions, the additional deficits are 0.0508, 0.626, and 0.732 parts per million. We then test a smooth power profile with a regular centre, a nearly flat intermediate rotation curve, and a finite outer limit. It fits DDO 154 and NGC 7814 at the level of the retained velocity errors, but does not reproduce the detailed structure of NGC 2403. Moving the prescribed outer turnover ten times farther away changes fitted speeds by less than 0.17 kilometres per second while changing the inferred remote power contrast substantially. An interference calculation translates the reconstructed deficits into equivalent amplitude and coherence requirements. The result connects galactic motion to the supporting-power gradients and collective scattering response that a galaxy model must supply.

Keywords: Operational Quantum Gravity; galactic rotation curves; supporting power; collective scattering; material response; dark matter

1 The physical question

Stars and gas orbit in a gravitational field whose radial strength is measured by their circular speeds. In the OQG account, that field originates in the electromagnetic exchange supporting matter. The question addressed here is concrete: how much must the supporting exchange change across a galaxy to produce the observed motion?

Matter in equilibrium receives and returns energy through its coupled charge and current responses. The incoming and outgoing powers balance, even though their common value can differ between environments. Surrounding matter scatters the shared field. On the gravitational branch developed in the OQG power-balance and scattering papers [1, 2], this changes the received exchange and lowers the balance sustaining the material state. Its clock rate, dimensions, and recoverable energy adjust together. The resulting energy gradient supplies the interaction; the material Hamiltonian generates the trajectory.

This sequence gives a useful way to study the galactic discrepancy usually described as dark matter. We first convert observed circular speeds into the required radial power contrast and compare it with the contribution assigned to observed gas and stars. We then choose a finite power profile and test whether its derivative reproduces the velocities. Reconstruction tells us what response is required, while a specified profile makes a prediction that can succeed or fail.

The supporting-power and matter-scaling theorems in Refs. [1–3] are the theoretical inputs. This paper determines their galactic requirements and tests one simple spatial profile. Deriving that profile and its parameters from the actual collective charge and current response of each galaxy remains the next source calculation. The established material correspondence and the galaxy-specific spatial response thus have distinct roles in the calculation.

2 From supporting exchange to orbital motion

Let P be the balanced supporting power of a complete receiving system and P_0 its value in a fixed comparison state. Both are positive powers. Let f be the ratio of corresponding transition frequencies and E_0 the complete reference rest energy. The supporting-power theorem [1, Section 4.3] gives

$$p \equiv \frac{P}{P_0} = f^2, \qquad \frac{E_{\text{rest}}}{E_0} = f = \sqrt{p}. \tag{1}$$

Power therefore determines the supported material energy through a square root. A small fractional reduction in power produces approximately half that fractional reduction in complete rest energy. The theorem compares states with fixed charge, matched current profiles, the same dimensionless equilibrium response, and correspondingly mapped spectra, dissipative channels, cutoffs, and correlations. At finite temperature, temperature scales with f. Appendix D gives the collective spectral argument.

Now move the system reversibly and adiabatically between two stationary environments, allowing its material state to follow local equilibrium. If p_1, p_2 are the endpoint ratios, the applied work and the force associated with rest-energy storage are

$$W_{1\to 2} = E_0\left(\sqrt{p_2} - \sqrt{p_1}\right), \qquad \mathbf{F}_{\text{rest}} = -E_0 \nabla \sqrt{p}. \tag{2}$$

The gradient ∇ measures spatial change in the fixed comparison coordinates. Moving toward greater support increases stored energy and requires positive applied work; the force points toward lower support. At a stationary endpoint the incoming and outgoing powers remain balanced, so the lower balance does not imply continuous loss of stored energy. On a steady circular orbit the conservative interaction redirects motion without acting as a drag power [2].

For galactic motion, use the weak, quasistatic material response and the reference propagation speed $c_0 = 299792.458\ \text{km s}^{-1}$. The Hamiltonian and inertia correspondence in Refs. [1–3] gives

$$\mathbf{g} \simeq -\frac{c_0^2}{2} \nabla \ln(P/P_0). \tag{3}$$

This is the working conversion from supporting-power gradient to acceleration. Equivalently, if Φ is potential energy per unit reference mass, then $\ln(P/P_0) \simeq 2\Phi/c_0^2$ up to a reference constant. The potential represents the material energy account.

For an axisymmetric galaxy, let r be radius in the disk plane and v_c the circular speed. Define s_P, the outward logarithmic power gradient, in units of inverse length. Circular balance gives

$$s_P(r) \equiv \frac{d\ln(P/P_0)}{dr}, \qquad v_c^2(r) \simeq \frac{c_0^2}{2}\, r\, s_P(r). \tag{4}$$

A positive outward gradient means less support inward and therefore an inward acceleration. The dimensionless slope is $d\ln P/d\ln r \simeq 2v_c^2/c_0^2$. Galactic speeds are small compared with c_0, so the

required fractional power changes are also small. Their gradients nevertheless produce the full measured orbital acceleration.

For orientation, consider an ideal flat curve with speed v_f. Relative to a reference radius r_m, integration gives

$$\frac{P(r)}{P(r_m)} \simeq \left(\frac{r}{r_m}\right)^{2v_f^2/c_0^2}, \qquad \ell(r;r_m) = \frac{2v_f^2}{c_0^2}\ln\frac{r_m}{r}. \tag{5}$$

Here ℓ is the positive logarithmic contrast between outer and inner balances. A speed of 200 km s^{-1} over one decade in radius requires a power deficit of only 2.0496 parts per million (ppm). Figure 1 shows its scale and direction. Setting the deficit to zero at the reference radius does not set the local acceleration to zero.

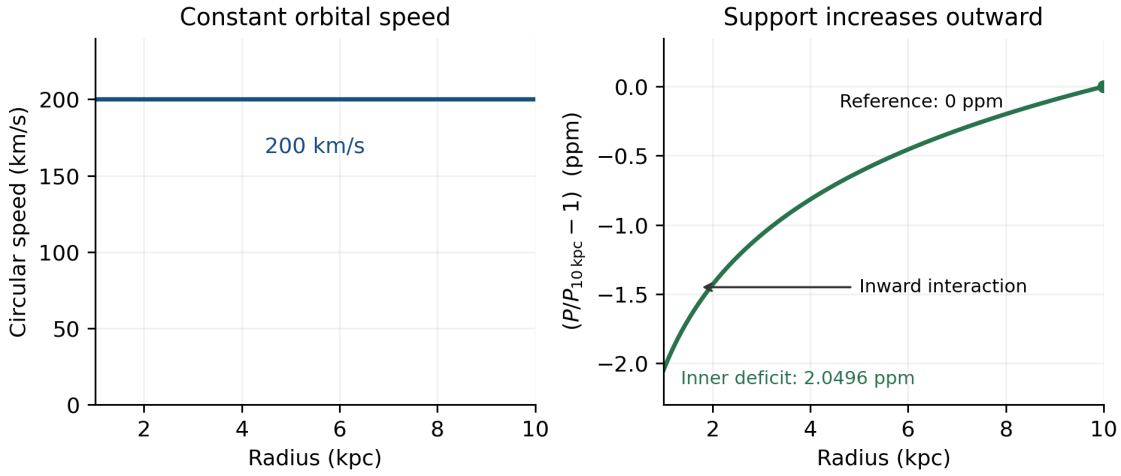

Figure 1. An illustrative flat rotation curve at 200 km/s, from 1 to 10 kpc. The right panel shows the supporting-power ratio relative to 10 kpc as a departure from unity in ppm. Support increases outward; the interaction points inward. This example establishes the scale of the conversion and is not a fit to a particular galaxy.

The reconstruction retains the leading weak-field response. Exponentiating its integral keeps power ratios positive and comparisons consistent; it does not add higher-order dynamics. The common material branch also identifies the power ratio with the full ambient stiffness ratio. Appendix A states that relation and its domain, including the distinction between clock and ruler factors.

3 Reconstructing the three galactic power profiles

We use published SPARC mass-model files [4] for DDO 154, NGC 2403, and NGC 7814: a gas-rich dwarf, a disk-dominated spiral, and a bulge-dominated system. Table 1 lists the adopted geometry and measured intervals. The underlying kinematic sources are Begeman et al. and Carignan and Beaulieu

for DDO 154 [5, 6], Daigle et al. and Fraternali et al. for NGC 2403 [7, 8], and Fraternali et al. for NGC 7814 [9]. All tabulated radii and velocities are retained.

Table 1. Adopted SPARC data. The last measured radius is r_m; kpc and Mpc denote kiloparsecs and megaparsecs. Geometry is held fixed.

Galaxy	Points	Distance (Mpc)	Inclination	Radius (kpc)
DDO 154	12	4.04	64°	0.49–5.92
NGC 2403	73	3.16	63°	0.16–20.87
NGC 7814	18	14.4	90°	0.63–19.53

Let v_{obs} be the inferred circular speed. Integrating Eq. (4) from an interior radius to r_m gives the observed logarithmic contrast and corresponding power ratio:

$$\ell_{\mathrm{obs}}(r; r_m) = \frac{2}{c_0^2}\int_r^{r_m} v_{\mathrm{obs}}^2(s)\,\frac{ds}{s}, \qquad q_{\mathrm{obs}} = e^{-\ell_{\mathrm{obs}}}. \tag{6}$$

The integration variable s is radius. Within the retained approximation, q_{obs} is $P(r)/P(r_m)$. We report the deficit $D_{\mathrm{obs}} = 1 - q_{\mathrm{obs}}$: one ppm means that inner support is one millionth below the balance at r_m. Both D_{obs} and ℓ_{obs} vanish at r_m by definition. These ratios are inferred from motion through OQG, rather than measured directly as exchanged watts.

The baryonic comparison uses SPARC's gas, disk, and bulge force components. Denote their tabulated velocity functions by V_g, V_d, V_b. With stellar mass-to-light ratios fixed at $\Upsilon_d = 0.5$ and $\Upsilon_b = 0.7$ in solar units at 3.6 micrometres, the signed force sum is

$$v_{\mathrm{bar}}^2 = V_g|V_g| + \Upsilon_d V_d|V_d| + \Upsilon_b V_b|V_b|. \tag{7}$$

Gas already includes SPARC's helium correction. Negative entries describe outward radial contributions and retain their sign. These are force components, not separate observed orbital speeds. Applying the same integral to v_{bar}^2 defines ℓ_{bar} and $q_{\mathrm{bar}} = e^{-\ell_{\mathrm{bar}}}$.

Denote the additional requirement relative to this fixed comparison by the subscript X. Logarithmic contrasts subtract, while power ratios divide:

$$\ell_X = \ell_{\mathrm{obs}} - \ell_{\mathrm{bar}}, \qquad q_X = \frac{q_{\mathrm{obs}}}{q_{\mathrm{bar}}} = e^{-\ell_X}, \qquad D_X = 1 - q_X. \tag{8}$$

With $D_{\mathrm{bar}} = 1 - q_{\mathrm{bar}}$, the exact decomposition in terms of deficits is

$$D_{\mathrm{obs}} = D_{\mathrm{bar}} + q_{\mathrm{bar}} D_X. \tag{9}$$

The factor q_{bar} matters conceptually even though it differs from unity by only a few ppm here. Subtracting ordinary deficits is only the small-deficit approximation.

Table 2 reports each contrast from the innermost data point to r_m. Uncertainties propagate only the tabulated velocity errors, treated as independent. Distance, inclination, mass-to-light ratios, and the baryonic force model are held fixed. Appendix C describes the integration and covariance of the cumulative profiles.

Table 2. Reconstructed inner-to-outer power deficits, in ppm. Uncertainties are one standard deviation from retained velocity errors. The baryonic column is a fixed comparison, not an uncertainty-free physical measurement.

Galaxy	Total deficit	Baryonic deficit	Additional deficit
DDO 154	0.06320 ± 0.00072	0.01242	0.05077 ± 0.00072
NGC 2403	0.98956 ± 0.00621	0.36391	0.62565 ± 0.00621
NGC 7814	4.28263 ± 0.15837	3.55091	0.73172 ± 0.15837

Figure 2 connects the velocities to their cumulative power contrasts. The additional logarithmic contrast contributes 80.3%, 63.2%, and 17.1% of the respective totals. Gas supplies 70.3% of the integrated baryonic contrast in DDO 154; the disk supplies 84.3% in NGC 2403; the bulge supplies 89.9% in NGC 7814. The examples test substantially different baryonic environments.

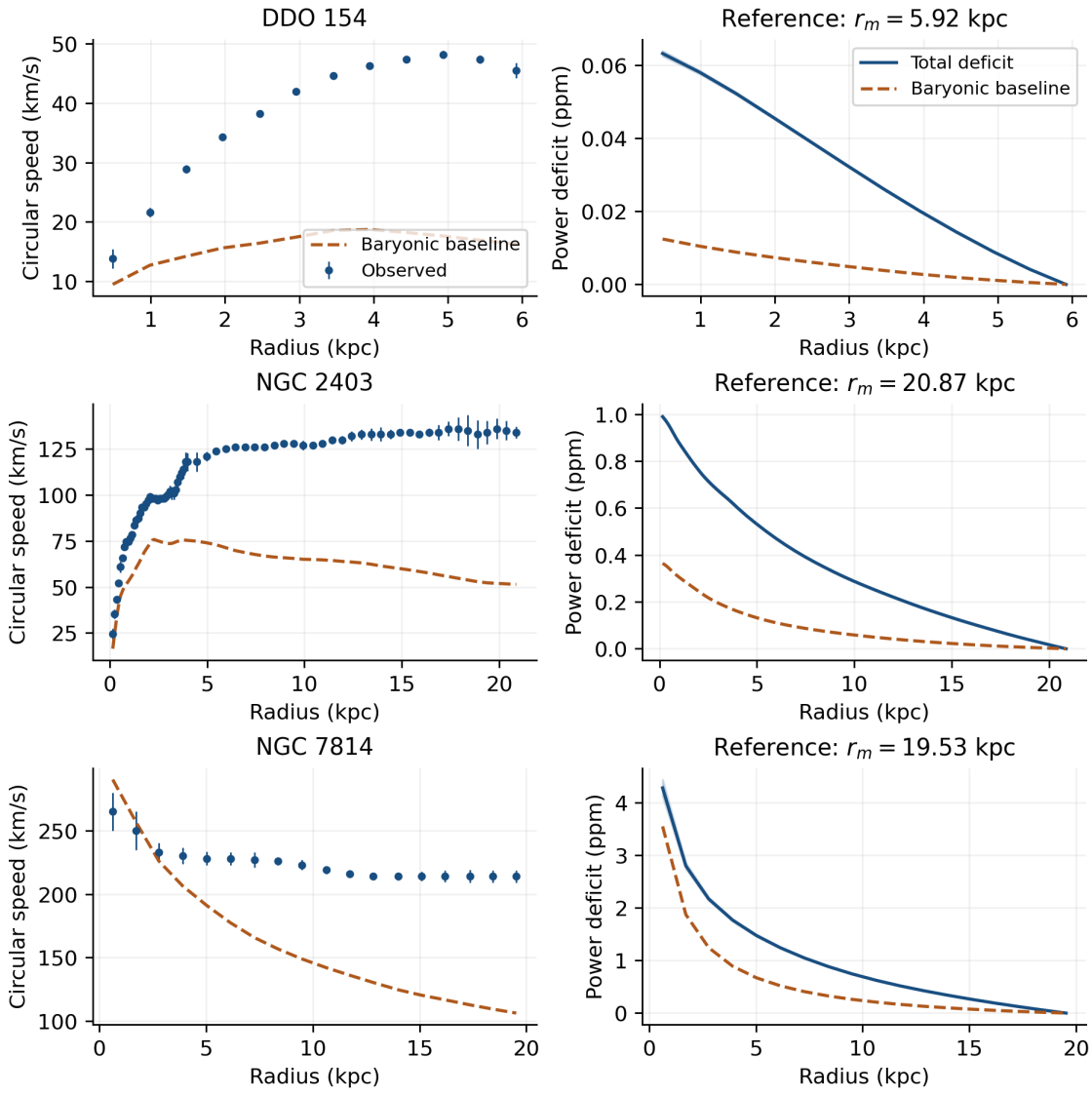

Figure 2. Left: observed circular speeds with tabulated errors and the adopted baryonic comparison. Right: total and baryonic deficits relative to each galaxy's last measured radius. Shading shows propagated velocity uncertainty; adjacent reconstructed points are correlated because their integrals overlap. Every curve reaches zero deficit at its reference radius while its gradient can remain nonzero.

In NGC 7814, $v_{\mathrm{obs}}^2 - v_{\mathrm{bar}}^2$ is negative at 0.63 and 1.72 kpc. These values are preserved. The cumulative additional contrast remains positive at every interior sample because the integration includes the rest of the interval. A local force discrepancy and an accumulated power contrast need not have the same sign at the same radius.

4 Testing a finite power profile

The reconstruction specifies what is required at measured radii. We now prescribe a smooth additional response and test its velocities. It has three readable scales: a speed V_s, a core radius r_c, and an outer turnover radius R_t, with $R_t > r_c > 0$. Set $\alpha = 2V_s^2/c_0^2$ and choose the additional logarithmic gradient

$$s_X(r) = \alpha \frac{r}{r^2+r_c^2} \frac{R_t}{\sqrt{r^2+R_t^2}}. \tag{10}$$

The first radial factor makes the response regular at the centre. The second makes it decline sufficiently fast to admit a finite remote reference. Substitution into Eq. (4) gives the additional squared speed and total model speed:

$$v_X^2 = V_s^2 \frac{r^2}{r^2+r_c^2} \frac{R_t}{\sqrt{r^2+R_t^2}}, \qquad v_{\text{model}}^2 = v_{\text{bar}}^2 + v_X^2. \tag{11}$$

For $r \ll r_c$, the additional speed rises approximately as $V_s r/r_c$. For $r_c \ll r \ll R_t$, it is nearly constant at V_s. For $r \gg R_t$, its square falls as $V_s^2 R_t/r$. Thus one profile joins a regular inner region, a flat intermediate region, and a finite outer tail. Appendix B supplies its closed-form integral and a finite, positive equivalent spherical mass representation.

Let $\tau_X(r)$ be the integral of s_X from r to infinity. The model comparison across the measured interval is

$$\ell_X^{\text{model}}(r; r_m) = \tau_X(r) - \tau_X(r_m), \qquad q_X^{\text{model}} = e^{-\ell_X^{\text{model}}}. \tag{12}$$

This subtraction separates the measured comparison from the unmeasured outer continuation. First prescribe $R_t = 10 r_m$ and fit V_s, r_c in velocity space. If $\sigma_{v,i}$ is the tabulated error at point i and N is the number of points, minimize

$$\chi^2 = \sum_{i=1}^{N} \left[\frac{v_{\text{model},i} - v_{\text{obs},i}}{\sigma_{v,i}}\right]^2, \qquad \chi^2_{\text{red}} = \frac{\chi^2}{N-2}. \tag{13}$$

The two fitted parameters account for $N - 2$ degrees of freedom. Geometry and baryonic parameters stay fixed, and no extra scatter is introduced. Table 3 and Figure 3 show the result; plotted residuals use the same model-minus-observed sign as Eq. (13).

Table 3. Fits with prescribed $R_t = 10r_m$. RMS is the root mean square velocity residual. Reduced chi-square is conditional on the adopted errors and fixed baryonic model.

Galaxy	V_s **(km/s)**	r_c **(kpc)**	R_t **(kpc)**	χ^2_{red}	**RMS (km/s)**
DDO 154	50.408	2.561	59.2	1.238	1.074
NGC 2403	116.127	3.145	208.7	19.694	6.929
NGC 7814	188.959	5.557	195.3	0.697	7.441

The profile describes DDO 154 and NGC 7814 at the level of the retained errors. NGC 2403 has substantial radial residual structure and rejects this two-parameter shape under the same fitting assumptions. It identifies where a more detailed spatial response is required. This tests the selected profile, rather than the supporting-power correspondence used to construct it.

Fitting velocities and integrating a reconstructed curve are different operations. The fitted inner-to-outer additional logarithmic contrasts are 0.05112, 0.57027, and 1.02295 ppm. Their differences from the direct reconstruction reflect the fitted shape and velocity-error weights. A satisfactory velocity statistic need not reproduce an integral exactly, especially where observational errors are broad.

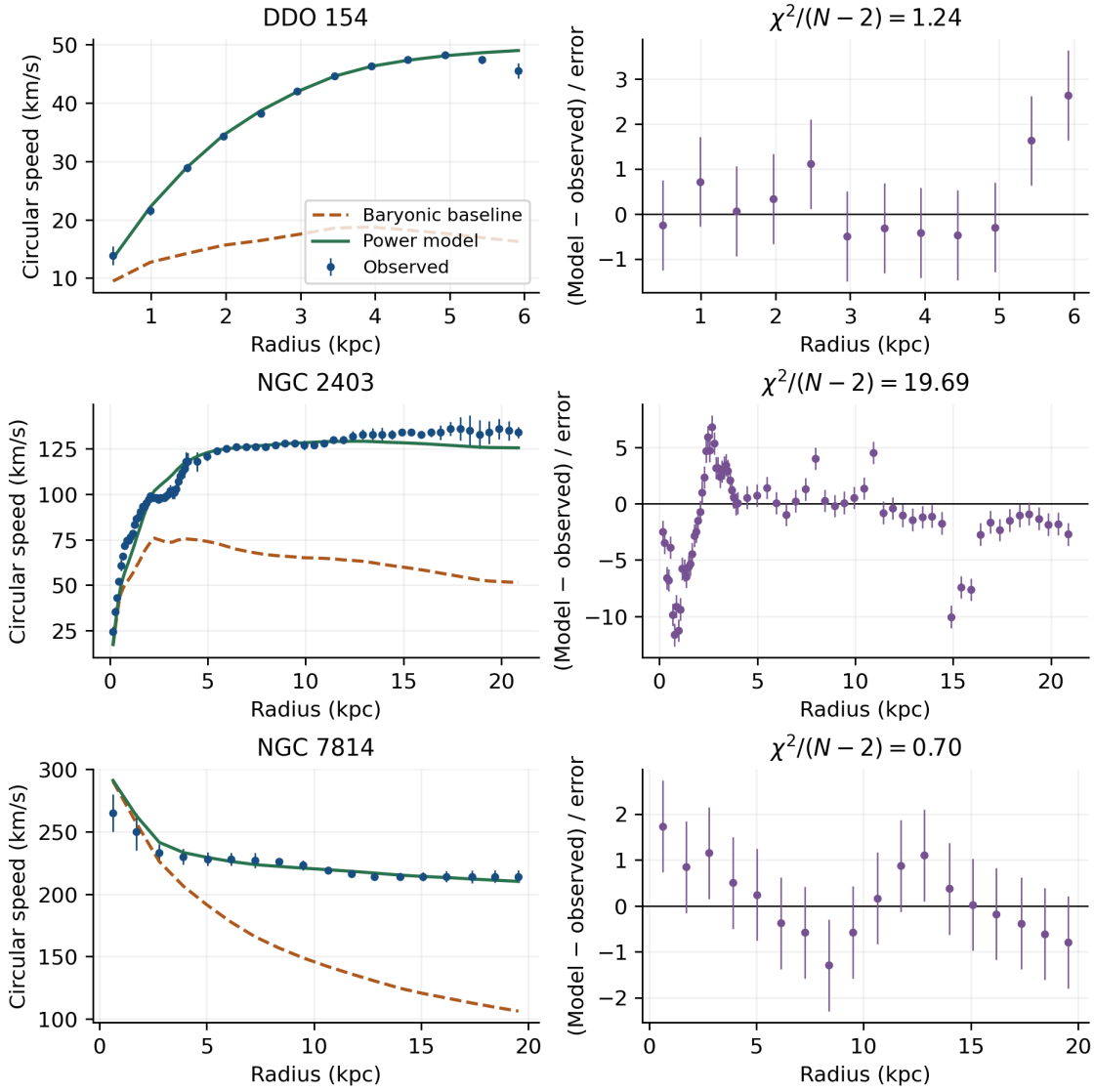

Figure 3. Left: finite supporting-power model, observed speeds, and baryonic comparison for $R_t = 10r_m$. Right: residuals $(v_{\text{model}} - v_{\text{obs}})/\sigma_v$ with unit error bars. NGC 2403 retains structured residuals despite broad agreement in speed scale. Each row reports its conditional reduced chi-square.

5 Connecting the measured interval to a remote reference

The last measured radius lies inside the same field that extends through the galactic environment. To compare an interior point with a remote limiting balance, fix an epoch t_* and let $P_\infty(t_*)$ denote that balance, if the global solution admits it. Define

$$p_\infty(r) = \frac{P(r)}{P_\infty}, \qquad \tau(r) = -\ln p_\infty(r), \qquad \tau_m = -\ln \frac{P(r_m)}{P_\infty}. \tag{14}$$

The epoch argument is suppressed after this definition. The unknown τ_m is the outer contrast between the measured edge and remote reference. With $q(r;r_m) = P(r)/P(r_m)$, ratio composition gives

$$p_\infty(r) = e^{-\tau_m} q(r;r_m), \qquad \tau(r) = \tau_m - \ln q(r;r_m). \tag{15}$$

This identity is exact for positive ratios. Comparisons through a galaxy, its group, and an intergalactic environment multiply in the same way. On the common material branch they also compare full ambient stiffness. Greater remote stiffness means a deeper contrast relative to that reference. The local rotation curve still depends on the spatial gradient: adding a constant τ_m alone cannot change the speed.

If a single conservative, weak, static radial description extends to the limiting reference, the required outer information is

$$\tau(r) \simeq \frac{2}{c_0^2}\int_r^\infty v_c^2\,(s)\,\frac{ds}{s}, \qquad \tau_m \simeq \frac{2}{c_0^2}\int_{r_m}^\infty v_c^2\,(s)\,\frac{ds}{s}. \tag{16}$$

Outside the measured interval, $v_c^2 = s\,d\Phi/ds$ denotes a radial force function, not necessarily an observed orbit. A nonzero flat curve continued forever makes this integral diverge. A finite limiting balance therefore requires an outer change of profile or a global cosmological matching prescription. The visible horizon itself supplies no material boundary condition.

Our chosen profile supplies one finite continuation. To demonstrate how weakly measured speeds determine its remote depth, we refit with the turnover moved from $10r_m$ to $100r_m$. Table 4 gives the change. Figure 4 illustrates NGC 2403, including its imperfect local fit. The outer curves are conditional model extensions.

Table 4. Sensitivity to the prescribed turnover. $\tau_X(r_m)$ is the additional logarithmic contrast from the last measured radius to infinity, in ppm. The last column is the greatest fitted-speed change at a measured radius after refitting.

Galaxy	$\tau_X(r_m), 10r_m$	$\tau_X(r_m), 100r_m$	**Maximum change (km/s)**
DDO 154	0.1648	0.2935	0.0353
NGC 2403	0.8965	1.5837	0.1680
NGC 7814	2.3521	4.1620	0.1214

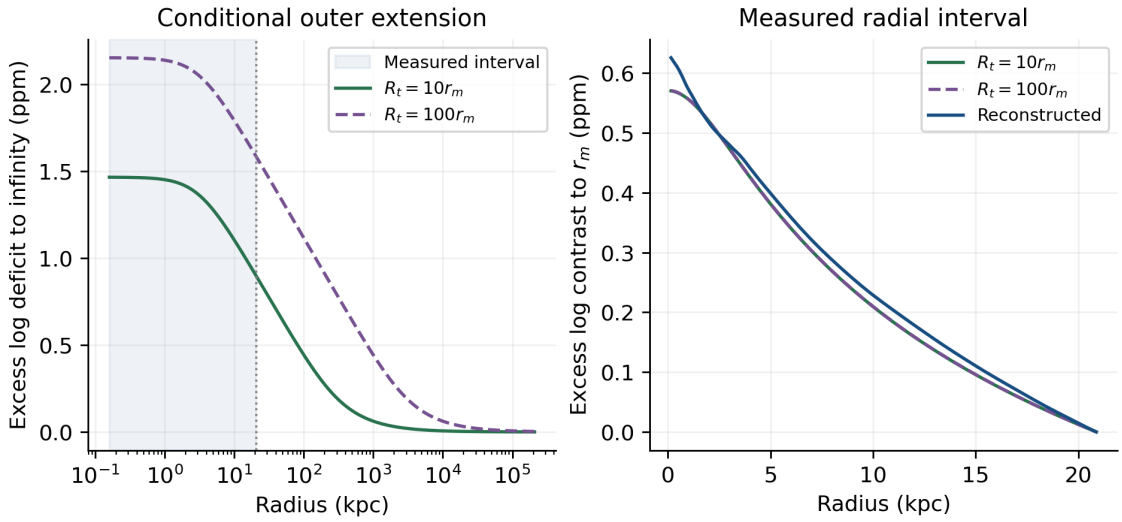

Figure 4. NGC 2403 with two prescribed turnover radii. Left: additional logarithmic contrast to infinity; shading marks the measured interval, beyond which the continuation is unmeasured. Right: both models normalized at the last measured radius, alongside the reconstructed contrast. Similar local gradients coexist with different outer depths. Only the additional component is shown; total remote depth also requires baryonic and environmental matching.

For a nonspherical environment, the local conservative relation is $\ln[P(b)/P(a)] \simeq -(2/c_0^2)\int_a^b \mathbf{g}\cdot d\mathbf{l}$, with compatible comparison standards. Galaxy-centred rotation data remove the acceleration of the centre and constrain internal motion. They do not specify the entire external vector field; differential external tides are neglected in these fits. Across cosmological regions, clocks, rulers, epochs, and response fields must be matched. The ratio identity in Eq. (15) remains useful when one radial integral to infinity is inappropriate.

Figure 5 makes the radial power profile visible as a surface over the disk plane. The two horizontal axes locate a point in the galaxy; both height and color show its supporting power. The lower central region therefore represents reduced support, with the outward gradient supplying the inward interaction. The flat map beneath repeats the same power contours. The normalization to a remote balance requires an explicit continuation beyond the observed radii.

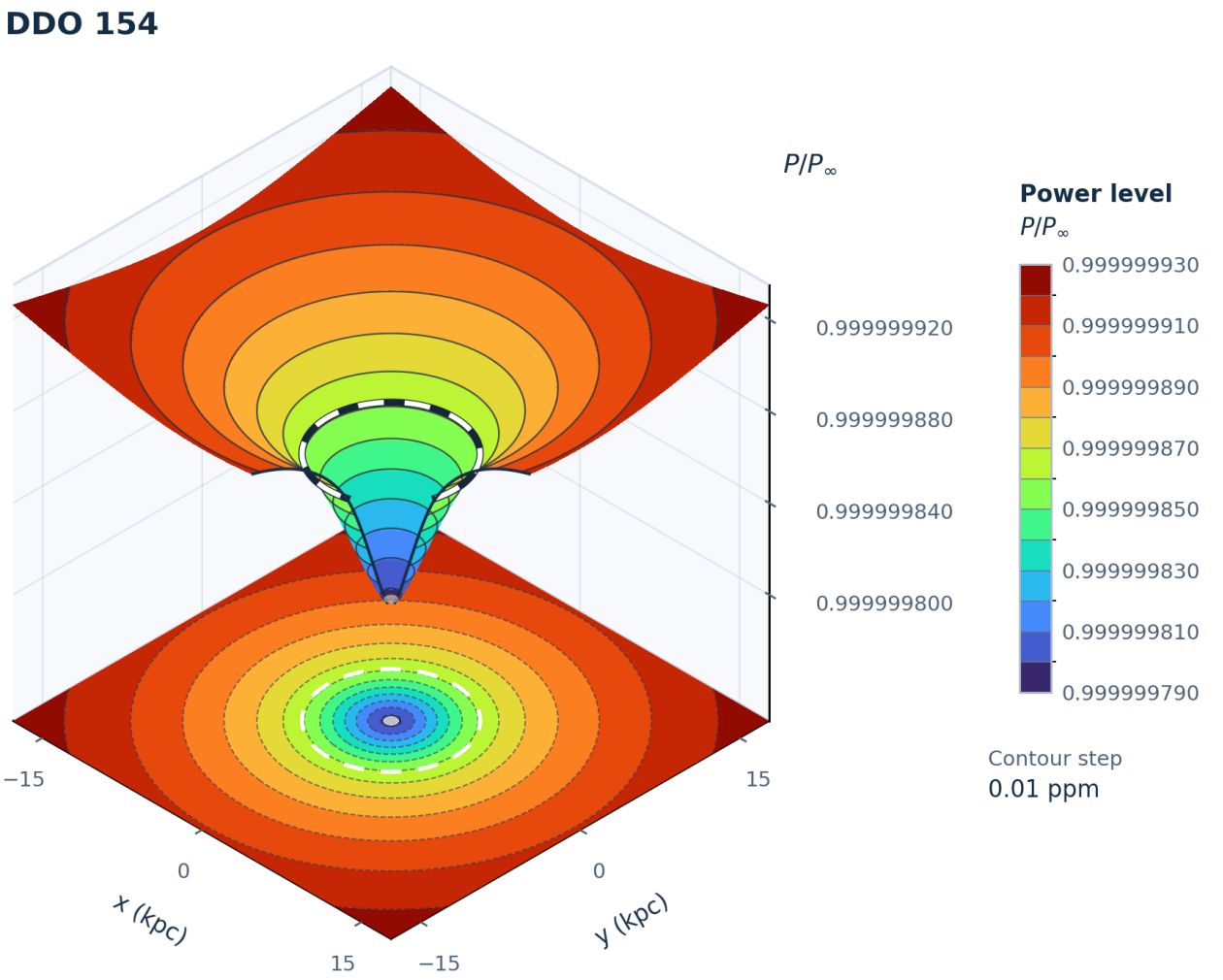

Figure 5. Total supporting power reconstructed from the 12 DDO 154 rotation samples, with an illustrative isolated-galaxy continuation. White dashes mark the last measured radius, $r_m = 5.92$ kpc; gray marks unresolved radii below 0.49 kpc. A 60-degree front sector is removed for visibility. Height is displayed as $10^6(P/P_\infty - 1)$, with true ratios on the axis; contour intervals are 0.01 ppm. Outside r_m, the continuation is $v_c^2(r) = v_m^2\sqrt{1 + (r_m/R_t)^2}/\sqrt{1 + (r/R_t)^2}$, where $v_m = 45.5$ km/s and $R_t = 10r_m = 59.2$ kpc. Its integral fixes the remote normalization, and P/P_∞ approaches 1 beyond the view. This total-power illustration differs from the additional-component fits in Figures 3 and 4.

6 What the deficits require of collective scattering

The physical source is the field received after contributions from surrounding charge and current responses combine. Their interference changes the balanced exchange. The collective supporting-power theorem [2] includes individual response and correlations between constituents. Those correlations and the receiving response determine the magnitude and spatial distribution of the supporting-power reduction. Appendix D states the collective balance.

We can translate the galactic deficits into amplitude requirements in a fixed reception norm: a quadratic measure of field amplitude weighted by the same receiver response, channels, and spectral convention. Let u be the reference amplitude, normalized by $\langle \| u \|^2 \rangle = 1$, and s its change. Brackets denote averaging in that norm. Define $\beta^2 = \langle \| s \|^2 \rangle$ and $C = \langle u^\dagger s \rangle$, where the dagger means complex conjugate transpose. The received-power ratio is

$$Q = 1 + \beta^2 + 2\mathrm{Re}C, \qquad |C| \le \beta. \tag{17}$$

The interference term $2\mathrm{Re}C$ can change power to first order even when the scattered contribution β^2 is very small. For a prescribed ratio, the triangle inequality gives

$$\beta \ge |1 - \sqrt{Q}|. \tag{18}$$

For a deficit $0 < Q \le 1$, the minimum occurs when the change is fully coherent and opposite to the reference: $s = -\eta u$. Then

$$\eta = 1 - \sqrt{Q}, \qquad Q = (1-\eta)^2, \qquad D = 1 - Q = 2\eta - \eta^2. \tag{19}$$

Set $Q = q_X$ to represent the additional galactic requirement in this fixed norm. Table 5 gives the minimum amplitude changes at the inner endpoints. Since D_X is small, $\eta \simeq D_X/2$. These are equivalent response amplitudes relative to the adopted baryonic comparison. The final column uses the coherence $\gamma = |C|/\beta$ for $\beta > 0$, with $0 \le \gamma \le 1$.

Table 5. Equivalent amplitude requirements. η^2 is the minimum added-field power fraction in the fixed norm. The coherence column is a necessary bound derived below, not measured coherence.

Galaxy	**η (ppm)**	**η^2**	**Minimum γ**

Galaxy	η (ppm)	η^2	Minimum γ
DDO 154	0.02539	6.44×10^{-16}	2.25×10^{-4}
NGC 2403	0.31282	9.79×10^{-14}	7.91×10^{-4}
NGC 7814	0.36586	1.34×10^{-13}	8.55×10^{-4}

For partial coherence, write $C = \gamma\beta e^{i\theta}$. Even at the most favourable phase, $\cos\theta = -1$, a deficit obeys

$$D \leq 2\gamma\beta - \beta^2 \leq \gamma^2, \qquad \gamma \geq \sqrt{D}. \tag{20}$$

The last inequality follows because the quadratic reaches its maximum at $\beta = \gamma$. The minimum amplitude in Table 5 requires full destructive coherence; weaker coherence generally requires a larger amplitude. An actual response calculation must satisfy both amplitude and correlation requirements. If a comparison instead has $q_X > 1$, its equivalent change is constructive relative to that baseline, without establishing that total support exceeds the ambient reference.

The reception norm is essential. Table 5 does not assert that every local electric or magnetic field amplitude falls by η. Under corresponding-state scaling, raw field strengths scale as f/b, where b is the length ratio, while receiving area scales as b^2. On the common branch $f = b$, raw field strengths can remain unchanged while integrated supporting power scales as f^2. Applying Eq. (19) across different receivers therefore requires mapping them to the same norm first.

The two-dipole calculation in Ref. [1, Section 2.3] explicitly reduces received power by 0.07546% at its stated parameters. Its fixed receiver and geometry differ from a galaxy's distributed response. A far-field intensity contribution proportional to $1/r^2$ is also distinct from the supporting-power contrast whose gradient produces a gravitational force. A galactic calculation must combine sources, correlations, propagation, and reception before extracting that contrast.

Source and receiver motion enter through the frequencies and correlations each body samples [2]. This analysis reconstructs a stationary, azimuthally averaged scalar profile from circular motion. A receiver's velocity-dependent factor cannot simply be added as extra stationary source power. Directional and rotational effects require their own response calculation before a galactic contribution can be assigned to them.

Figure 6 expresses the same total DDO 154 profile and outer continuation as Figure 5 through the equivalent amplitude in Eq. (19), using $Q = P/P_\infty$. The supporting-power depression becomes a positive amplitude peak. The scaled stellar illustration and top view show how far the prescribed response extends beyond the adopted optical body.

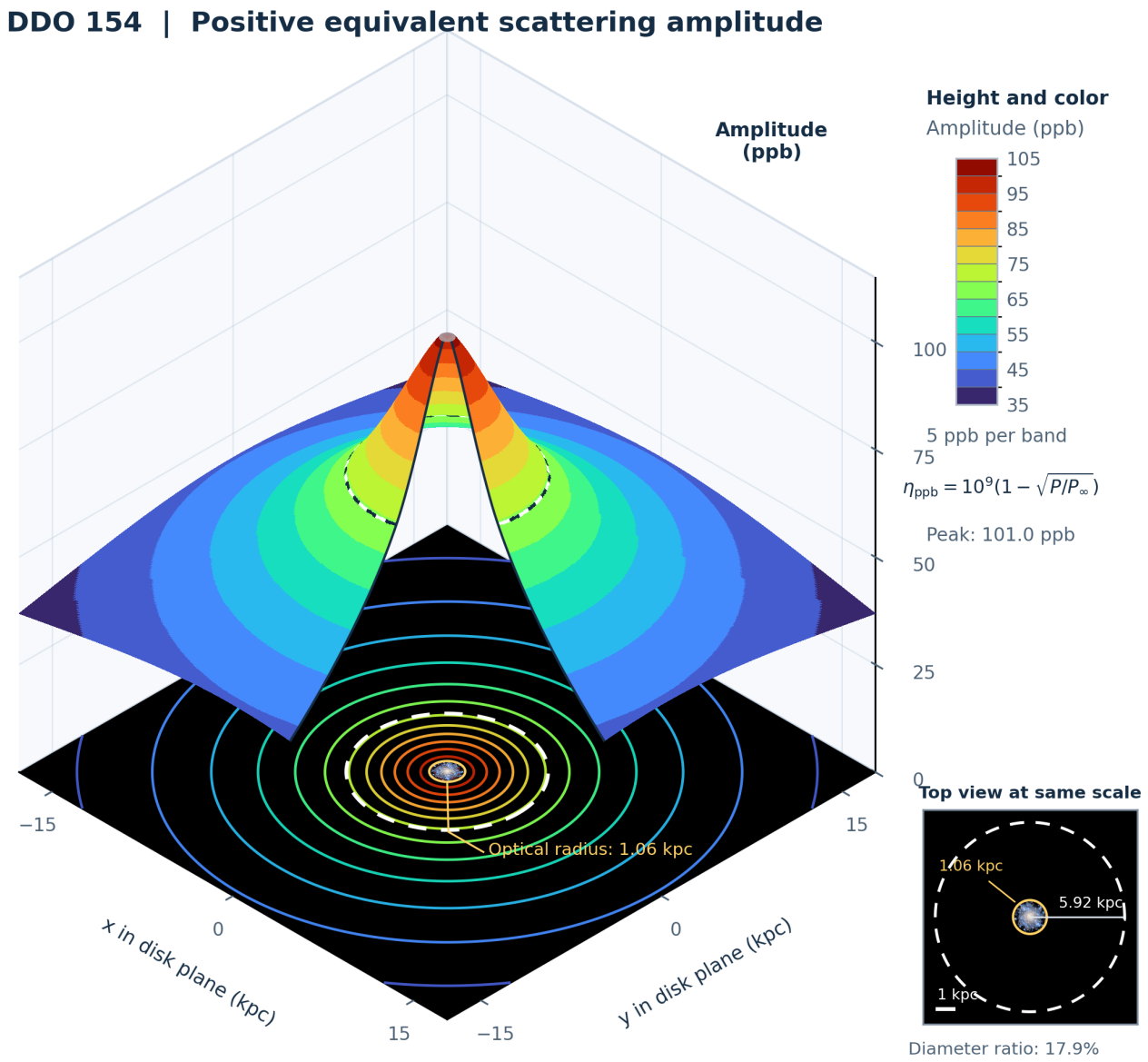

Figure 6. Positive equivalent scattering amplitude $\eta_{\mathrm{ppb}} = 10^9\left(1 - \sqrt{P/P_\infty}\right)$ for the total profile in Figure 5. Height and color show the same minimum fully coherent opposing amplitude in the fixed reception norm of Section 6; the resolved peak is 101.0 ppb and the bands are 5 ppb apart. The vertical scale is exaggerated. The AI-generated stellar illustration is sized to an adopted optical diameter of 2.12 kpc, using $D_{25} = 1.8$ arcmin [6, Table 4] at 4.04 Mpc. Its 1.06 kpc radius is marked in gold. The white dashed ring has radius 5.92 kpc and diameter 11.84 kpc; the optical-to-ring diameter ratio is 17.9%. Gas and fainter stars can extend beyond this optical guide. Gray marks unresolved radii below 0.49 kpc. Beyond the measured ring, the same prescribed continuation fixes the remote normalization. This total-profile amplitude uses a different reference from the additional-component amplitudes in Table 5.

7 Interpretation and conclusions

The principal result is a practical map from galactic motion to OQG supporting exchange. Observed speeds determine a logarithmic power gradient. Its integral gives contrasts of 0.0632–4.28 ppm across the measured intervals, with 0.0508–0.732 ppm additionally required relative to the adopted gas and stellar contributions. The amplitude calculation expresses the same requirements in a fixed reception norm, connecting observations to the collective scattering account.

The finite profile demonstrates a response that is regular centrally, supports an extended nearly flat curve, and approaches a finite remote balance. Its fits to DDO 154 and NGC 7814, and its failure on the detailed structure of NGC 2403, provide useful discrimination. The next galactic source model should calculate the spatial response and its parameters from the distribution and correlations of matter, then test its velocities using the same reconstruction and residual checks.

The baryonic comparison remains consequential. A 10% increase in NGC 7814's bulge mass-to-light ratio increases its integrated baryonic logarithmic contrast by 0.3194 ppm, about 44% of the current additional contrast. Uniform distance rescaling leaves the observed integral at corresponding fractional radii unchanged, but changes physical lengths and the baryonic model. Inclination changes the velocity scale through $v \propto 1/\sin i$. These effects belong in physical parameter uncertainties for a larger sample.

Local motion determines gradients more directly than remote depth. Increasing the prescribed turnover tenfold changes fitted speeds by less than 0.17 km/s while substantially shifting the outer contrast. Additional information can constrain that boundary: within the same weak static normalization, escape speed gives $\tau \simeq v_{\mathrm{esc}}^2/c_0^2$, and corresponding clock comparisons give $P_2/P_1 = (f_2/f_1)^2$. Lensing comparisons require the full propagation and material response, rather than a rotation-curve integral alone.

Together, the reconstruction, finite-profile test, and interference bounds specify the magnitude, spatial form, and collective-response requirements of a galactic OQG account. They turn the observed discrepancy into a quantitative source problem with explicit inputs, outputs, and tests.

Appendix A. Power and full ambient stiffness

The common material branch links power to full ambient stress stiffness. Let b be the ratio of corresponding lengths and f the frequency ratio of Section 2. Write $A = A^{\mathrm{tot}}_{2,E}$ for the completed transverse, traceless quadratic stress-response coefficient, with units of energy squared. The subscript E denotes the Euclidean response convention, not an epoch. With $\hbar$ the reduced Planck constant and G the gravitational coupling, Ref. [1, Section 4.4] gives

$$A = \frac{\hbar c^5}{32\pi G}, \qquad \kappa \equiv \frac{G}{c^4} = \text{constant}, \qquad \frac{A}{A_0} = \frac{c}{c_0} = fb. \tag{21}$$

The total coefficient includes the ambient reference and matched material contributions. A state-dependent increment cannot replace it. It is not an ordinary mechanical bulk modulus. On the common branch $f = b$, the linked ratios are

$$\frac{A}{A_0} = \frac{c}{c_0} = p, \qquad \frac{\epsilon}{\epsilon_0} = \frac{\mu}{\mu_0} = p^{-1}, \qquad \frac{G}{G_0} = p^4. \tag{22}$$

Permittivity ϵ and permeability μ increase together as support falls, leaving wave impedance unchanged. Corresponding capacitance and inductance scale as $p^{-1/2}$. These comparisons use fixed standards; locally rescaled measuring devices must be accounted for separately.

Independent clock and ruler factors must be retained outside this branch. In the exact spherical construction of Ref. [1, Section 8], $p = f^2$ still holds while $A/A_0 = fb$, and the two ratios need not coincide. The equality used for the galactic reconstruction is the common weak-field response at the retained order.

Appendix B. Finite outer integral and equivalent mass

Define $d = \sqrt{R_t^2 - r_c^2}$, real because $R_t > r_c$. The profile in Section 4 integrates explicitly from r to infinity:

$$\tau_X(r) = \alpha \, \frac{R_t}{d} \operatorname{asinh}\left(\frac{d}{\sqrt{r^2 + r_c^2}}\right). \tag{23}$$

Differentiation gives $-d\tau_X/dr = s_X$. The expression is finite at the centre and tends to zero at infinity, so $e^{-\tau_X}$ has the required positive outer normalization. The inverse hyperbolic sine form avoids subtracting nearly equal terms numerically.

A useful force diagnostic is the equivalent spherical mass $M_X = rv_X^2/G_0$, where G_0 is the reference gravitational coupling. This represents the additional radial acceleration without asserting an additional particle population. It gives

$$M_X(r) = \frac{V_s^2 R_t}{G_0} \frac{r^3}{(r^2+r_c^2)\sqrt{r^2+R_t^2}}, \qquad M_X(\infty) = \frac{V_s^2 R_t}{G_0}. \tag{24}$$

The mass is positive and increasing. For $r > 0$, its logarithmic derivative is $2r_c^2/[r(r^2 + r_c^2)] + R_t^2/[r(r^2 + R_t^2)] > 0$. It grows as r^3 near the centre and approaches the finite limit in Eq. (24).

When $r, r_c \ll R_t$, the same expressions reduce to

$$\tau_X(r) \simeq \alpha \ln \frac{2R_t}{\sqrt{r^2+r_c^2}}, \qquad v_X^2(r) \simeq V_s^2 \frac{r^2}{r^2+r_c^2}. \tag{25}$$

Increasing R_t by a factor λ adds approximately $\alpha \ln \lambda$ to remote depth while barely changing the local speed. This explains Table 4. Total depth additionally requires a continuation of the baryonic and environmental contributions.

Appendix C. Numerical integration, errors, and reproducibility

The reconstruction uses piecewise-linear squared speed as a function of $x = \ln r$. Let w_{ij} be the trapezoidal weight of sample j in the integral from sample i to the last sample. Then

$$\ell_i = \frac{2}{c_0^2} \sum_j w_{ij}\, v_j^2, \qquad J_{ij} \equiv \frac{\partial \ell_i}{\partial v_j} = \frac{4}{c_0^2} w_{ij} v_j. \tag{26}$$

Each interval contributes half its logarithmic width to each endpoint. The last weight row is zero. With independent input velocity errors $\sigma_{v,j}$, first-order propagation gives

$$\mathrm{Cov}(\ell_i, \ell_k) = \sum_j J_{ij} J_{kj} \sigma_{v,j}^2, \qquad \sigma_{D,i} = e^{-\ell_i} \sigma_{\ell,i}. \tag{27}$$

The same logarithmic uncertainty applies to ℓ_X while the baryonic baseline is fixed. For amplitude, $\sigma_{\eta,i} = 1/2\, e^{-\ell_i/2}\sigma_{\ell,i}$. Overlapping integrals produce covariance between reconstructed radii; full matrices accompany the radial tables. Stable evaluations use $D = -\mathrm{expm1}(-\ell)$ and $\eta = -\mathrm{expm1}(-\ell/2)$ to preserve precision near unity.

Fits minimize Eq. (13) using logarithmic parameters. The speed bounds are 10^{-3} to 10^{4} km/s; the core-radius bounds are 10^{-5} kpc to $0.99R_t$. Six starts combine $V_s = 50{,}150{,}300$ km/s with $r_c = r_{\mathrm{inner}}, r_m/2$. Relative convergence tolerances are 10^{-12}, with at most 4,000 function evaluations per run. The best converged result is retained; no reported optimum lies near a bound. The archive records the multistart spread and both turnover fits.

Checks recover the analytic flat-curve integral, exact endpoint normalization, logarithmic and deficit decomposition, interval derivatives, interference identity, and velocity-error Jacobian. They verify covariance symmetry and positive semidefiniteness, the outer integral against independent quadrature to infinity, its derivative against the speed profile, ratio composition, and monotonic convergence of equivalent mass. The version 0.6 reconstruction and fits reproduce the preceding calculation to numerical precision.

The supplementary archive contains unmodified SPARC inputs and checksums, numerical scripts and results, the figure generator, this manuscript source, and the Word builder. Calculations and figures regenerate offline once dependencies are installed. The builder requires Pandoc and produces native editable equations. Equation labels resolve automatically, and a manifest records the package files.

Appendix D. Collective exchange and the reception norm

Let **Q** collect the relevant charge coordinates, $S_Q(\nu)$ their symmetrized two-sided spectral matrix, and $R(\nu)$ the Hermitian dissipative response in the receiving channels. Here ν is angular frequency. Off-diagonal spectral entries contain correlations between coordinates. The balanced exchange is [1, 2]

$$P = \int_{-\infty}^{\infty} \frac{d\nu}{2\pi}\, \nu^2 \mathrm{Tr}[R(\nu)S_Q(\nu)] = P_{\mathrm{in}}. \tag{28}$$

The trace contracts the coupled receiving channels. For the passive response used here, the quadratic form supplies a nonnegative power measure. Nuclear binding and the complete coupled response remain within the receiving system; this expression does not replace them with uncoupled classical dipoles.

Under the corresponding-state map, $R_f(f\nu) = R_0(\nu)$ and $S_{Q,f}(f\nu) = f^{-1}S_{Q,0}(\nu)$. Changing integration variable gives one factor of f from the measure, two from squared frequency, and one inverse factor from the spectrum. Thus the complete exchange scales as f^2, including correlations satisfying the same map. This is the collective form of Eq. (1). Matched channels, spectra, cutoffs, and equilibrium states define the theorem's domain.

Section 6 represents changes after receiver weighting and spectral conventions have been fixed or mapped to a common comparison. Cauchy–Schwarz gives $|C| \leq \beta$, and the reverse triangle inequality gives Eq. (18). These are necessary amplitude and coherence conditions. Evaluating the actual galactic response requires its spectral correlations and receiving operator; the tabulated equivalent amplitudes are targets for that calculation.

Statements and Declarations

Funding. This work was self-funded by the author. No funds, grants, or other external support were received during the preparation of this manuscript.

Conflict of Interest. On behalf of all authors, the corresponding author states that there is no conflict of interest.

Author contributions. Todd J. Desiato conceived the OQG program and the material-scaling interpretation, directed the theoretical development, reviewed the calculations and literature, and prepared the manuscript.

Data availability. This study uses published SPARC data [4]; no new experimental or observational datasets were generated. The supplementary archive contains the three unmodified mass-model files, source tables, original downloaded archive, input checksums, and generated numerical results. Public source data remain available at https://astroweb.case.edu/SPARC/.

Code availability. The supplementary archive contains the reconstruction and fitting scripts, numerical verification, figure generator, manuscript source, and Word-document builder, with instructions and dependencies for reproduction.

Ethics approval and consent to participate. Not applicable. This study involved no human participants, human data, animals, or biological material.

Consent for publication. Not applicable.

Use of generative artificial intelligence. The author used OpenAI ChatGPT and Codex for literature discovery, mathematical cross-checking, numerical evaluation, organization, drafting, and editing. The author is responsible for reviewing the scientific arguments, equations, references, and final text and for the content of the manuscript.

Supplementary information. The separate calculation package is supplied as OQG_Paper_56_Reproducibility_V0_6.zip. It contains the data, code, source manuscript, figures, and verification records described above.

References

[1] Desiato, T. J. (2026). *Operational Quantum Gravity: From Electromagnetic Power Balance to Gravitational Response*. Manuscript, version 2.3, 21 October 2026. Sections 2.3, 4.3–4.4, 5–8.

[2] Desiato, T. J. (2026). *Scattering as the Cause of Gravity in Operational Quantum Gravity*. Manuscript, version 1.1, 23 October 2026.

[3] Desiato, T. J. (2026). *Matter Wave Scaling and Recoverable Energy Storage in Operational Quantum Gravity*. Manuscript, version 1.5, 21 October 2026.

[4] Lelli, F., McGaugh, S. S., Schombert, J. M. (2016). SPARC: Mass models for 175 disk galaxies with Spitzer photometry and accurate rotation curves. *The Astronomical Journal*, 152, 157. https://doi.org/10.3847/0004-6256/152/6/157. Data: https://astroweb.case.edu/SPARC/ (Rotmod_LTG.zip, SPARC_Lelli2016c.mrt, and MassModels_Lelli2016c.mrt; retrieved 12 October 2026).

[5] Begeman, K. G., Broeils, A. H., Sanders, R. H. (1991). Extended rotation curves of spiral galaxies: dark haloes and modified dynamics. *Monthly Notices of the Royal Astronomical Society*, 249, 523–537. https://doi.org/10.1093/mnras/249.3.523

[6] Carignan, C., Beaulieu, S. (1989). Optical and H I studies of the “gas-rich” dwarf irregular galaxy DDO 154. *The Astrophysical Journal*, 347, 760–770. https://doi.org/10.1086/168167

[7] Daigle, O., Carignan, C., Amram, P., Hernandez, O., Chemin, L., Balkowski, C., Kennicutt, R. (2006). Hα kinematics of the SINGS nearby galaxies survey – I. *Monthly Notices of the Royal Astronomical Society*, 367, 469–512. https://doi.org/10.1111/j.1365-2966.2006.10002.x

[8] Fraternali, F., van Moorsel, G., Sancisi, R., Oosterloo, T. (2002). Deep H I survey of the spiral galaxy NGC 2403. *The Astronomical Journal*, 123, 3124–3140. https://doi.org/10.1086/340358

[9] Fraternali, F., Sancisi, R., Kamphuis, P. (2011). A tale of two galaxies: light and mass in NGC 891 and NGC 7814. *Astronomy & Astrophysics*, 531, A64. https://doi.org/10.1051/0004-6361/201116634